Available online at www.sciencedirect.com
ScienceDirect
International Journal of Multiphase Flow 32 (2006) 1219–1233
International Journal of Multiphase Flow
www.elsevier.com/locate/ijmulflow

Effect of the phase transition on intra-tow flow behavior and void formation in liquid composite molding

N. Yamaleev [a,*], R. Mohan [b,*]

[a] Department of Mathematics, North Carolina A&T State University, Greensboro, NC 27411, USA
[b] Computational Science and Engineering, Mechanical Engineering, Center for Advanced Materials and Smart Structures, North Carolina A&T State University, Greensboro, NC 27411, USA

Received 12 July 2005; received in revised form 17 May 2006

Abstract

A model describing the microscopic isothermal flow inside a fiber bundle completely surrounded by a resin during a liquid molding process is developed. A distinguishing feature of this model is that it takes into account the liquid/vapor phase transition occurring in the gas entrapped inside the tow. In contrast to the existing void formation models which assume that the entrapped gas behaves as an ideal gas, in the present analysis, the condensation and vaporization processes inherent in the liquid/vapor system under high external pressures are simulated by using the Peng–Robinson equation of state. The numerical results show that the phase transition inside the fiber tow has strong effect on both the void dynamics and its size, thus indicating the need to account for this phenomenon in simulation of liquid composite molding processes.

Keywords: Void formation; Intra-tow flow; Peng–Robinson equation; Resin transfer molding; Porous medium

1. Introduction

Liquid composite molding (LCM) processes such as the resin transfer molding (RTM) and its variants are routinely used for the production of net-shape structural polymer composite materials. During infusion of a reactive polymeric resin permeating a dry fiber preform inside a complex mold cavity, the macroscopic resin flow through the fiber preform and inter-tow gaps is simultaneously accompanied by the microscopic impregnation of individual fiber bundles (tows), made up of 10^2–10^3 individual fibers, as shown in Fig. 1. Though the manufacturing process is generally considered to be successful in the absence of large dry-spot regions, the accompanying infusion through the individual fiber bundles can lead to appearance of un-wetted fibers, potentially causing voids. The void formation can occur on the length scales of both individual fibers and fiber bundles. The process induced voids, if not removed, become a part of the composite structure and adversely

* Corresponding authors. Tel.: +1 336 334 7822 (N. Yamaleev), +1 336 256 2408 (R. Mohan).
E-mail addresses: nkyamale@ncat.edu (N. Yamaleev), rvmohan@ncat.edu (R. Mohan).

0301-9322/$ - see front matter
doi:10.1016/j.ijmultiphaseflow.2006.05.011

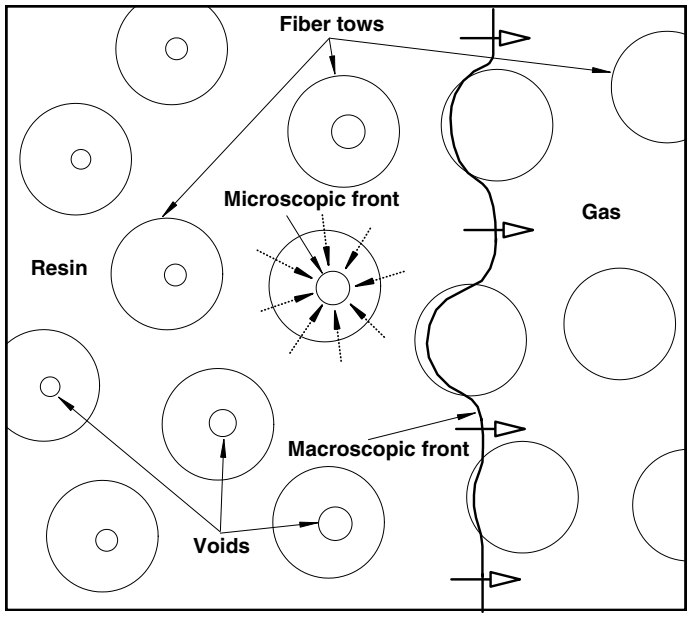

Fig. 1. A schematic of the gas entrapment mechanism in fiber bundles.

impact on the mechanical and service properties of the processed composite. Most of the models available in the literature (Mohan et al., 1999; Ngo et al., 1998; Bruschke and Advani, 1990; Lin et al., 1993; Trouchu et al., 1993) simulate the macroscopic flow through a fibrous porous media, using Darcy's law. Although these models have been successfully used for predicting the macroscopic flow characteristics, understanding of the physical phenomena associated with the accompanying flow infusion inside fiber bundles and its interaction with the surrounding macroscopic flow will provide further insight into mechanisms and behavior governing the void formation. The quantitative simulation and prediction of the void formation are important for proper design and selection of material and processing parameters to minimize such voids in the composite materials.

Several models have been developed for simulation of void formation in RTM (Parnas and Phelan, 1991; Pillai and Advani, 1998; Wood and Bader, 1994; Lundstrom, 1997). Parnas and Phelan (1991) explained the air entrapment inside fiber tows as a result of the difference in the permeabilities of the intra-tow and inter-tow regions. Because the interstitial space inside a fiber bundle is much smaller than the space between bundles themselves, the flow front is able to reach the downstream sides of the tow before the gas inside the tow can be forced out by the resin impregnation process. This delayed impregnation is incorporated into the governing macroscopic flow equations by adding a so-called "sink" term to the continuity equation. In Parnas and Phelan (1991), it is assumed that the air entrapped inside the tow follows the ideal gas law. As a result, the pressure inside the air "bubble" rapidly increases as the microscopic resin front moves into the tow from the perimeter and eventually becomes equal to the exterior pressure. Hence, the pressure balance is achieved at a non-zero value of the void volume at which the local pressure gradient is equal to zero. The zero pressure gradient does not permit further flow inside the tow, thus leaving the entrapped air as a void.

A similar model using the "sink" term in the continuity equation is studied in Pillai and Advani (1998). As pointed out in this paper, the use of the ideal gas law for air entrapped inside a fiber tow significantly reduces the liquid absorption by the tow, leading to a qualitatively different inlet pressure behavior as compared with that observed in the experiments. To overcome this problem, the "sink" term in Pillai and Advani (1998) is assumed to be either a constant or a step function, i.e., the sink absorbs liquid from the inter-tow region for a limited period of time until it becomes fully saturated. Although this on/off type constant sink provides better agreement with the experimental data, the physical flow phenomena that take place at the microscopic level have not been identified and explained, leading to ambiguity in determining the time taken to fill the intra-tow region, which is one of the major parameters used in the model presented in Pillai and Advani (1998).

Another class of models describing the void dynamics during RTM has been developed in Wood and Bader (1994) and Lundstrom (1997). These models are based on the mass diffusion theory and predict the growth and collapse of pre-existing gas bubbles during the process cycle. In these papers, the applicability of the diffusion theory is investigated, and the required input parameters for the diffusion models were measured experimentally. As follows from these studies, the void radius decreases at relatively slow rate, and the void disappears in the order of minutes due to the diffusion. One of the main assumptions used in these models is that voids are very small and have a spherical shape which is comparable with the fiber radius. As a result, the characteristic time scale for the diffusion can be estimated as follows:

$$\frac{r_f^2}{D} \sim \frac{(5 \times 10^{-6})^2 \text{ m}^2}{10^{-12} \text{ m}^2/\text{s}} = 25 \text{ s},$$

where D is the diffusion coefficient of the resin. However, for the tow impregnation process, the initial void radius is of the order of the tow radius, and the time required for the void to dissolve becomes

$$\frac{r_t^2}{D} \sim \frac{(10^{-4})^2 \text{ m}^2}{10^{-12} \text{ m}^2/\text{s}} = 10^4 \text{ s},$$

which could be longer than the molding process itself. The above consideration indicates that the diffusion model is applicable for predicting the final stage of the void formation process, and cannot be used to describe the initial void dynamics.

In contrast to the models presented above, we propose a model that takes into account the phase transition occurring in the multi-component gas mixture entrapped inside fiber bundles during RTM. In the present analysis, the behavior of the multiphase mixture inside a fiber bundle is described by the Peng–Robinson equation of state. Because the phase transition occurs on the time scale of less than one second, the present model predicts the initial void formation and dynamics. Similar to the model developed by Parnas et al. the void dynamics in the present work is determined by the pressure gradient at the interface between the gases entrapped inside a fiber bundle and the surrounding resin. As the void size decreases, the pressure gradient decreases becoming eventually equal to zero. When the pressure gradient inside the tow vanishes, the diffusion becomes a dominant process that determines the void size dynamics. Note that because of the 2–3 orders of magnitude difference in the temporal scales associated with the phase transition and molecular diffusion, these two processes can be simulated in a decoupled manner, and the void size predicted by our model can be used as an initial condition for the diffusion-based models developed in Wood and Bader (1994) and Lundstrom (1997). The numerical results have shown that the phase transition inside fiber tows has strong influence on both the void size and pressure, thus indicating the need to account for this phenomenon in simulation of LCM processes.

2. Model for void formation in LCM

The above discussions clearly indicate that a more accurate modeling and a deeper physical understanding of the flow behavior inside fiber bundles are needed. The main objective of this paper is to develop a model for the intra-tow flow through a fiber bundle that accounts for not only the macroscopic pressure field around the tow and the surface tension effects, but also a very important physical process associated with the gas–liquid phase transition. This phenomenon should be taken into account to quantitatively predict the intra-tow flow dynamics. Note that the vapor–liquid phase transition has not been considered in the models developed previously (Parnas and Phelan, 1991; Pillai and Advani, 1998; Wood and Bader, 1994; Lundstrom, 1997).

The void formation mechanism studied in the present work is similar to one proposed in Parnas and Phelan (1991). The main idea of this model is based on the observation that the permeability coefficient of a preform, associated with the macro-flow between tows, is much greater than that of a fiber bundle, associated with the micro-flow inside the tow. Therefore, as the advancing macroscopic resin flow front encounters a fiber bundle, it flows around the tow, entrapping a pocket of gas that we will call a bubble. A schematic of this process is shown in Fig. 1. After the macro-front surrounds and bypasses the bundle, the fiber tow is slowly impregnated with the fluid. Because the fiber radius r_f is about two orders of magnitude less than the tow radius r_t, the

microscopic flow inside the fiber bundle consisting of 10^2–10^3 individual fibers can be treated as a flow in a porous medium. Without including the thermal and cure effects, the intra-tow flow can be described by the conservation of mass equation and the Darcy's law for momentum balance:

$$\nabla \cdot \mathbf{V} = 0, \tag{1}$$

$$\mathbf{V} = -\frac{\mathbf{K}}{\mu}\nabla P, \tag{2}$$

where $\mathbf{V}$ is the Darcian volume-averaged velocity vector of the fluid inside the bundle, $\mathbf{K}$ is the permeability tensor of the fiber bundle, μ and P are the fluid viscosity and pressure, respectively.

Assuming that the tow is a cylinder, and the microscopic flow is cylindrically symmetrical, only the diagonal terms K_{xx} and K_{rr} of the permeability tensor are non-zero. Under these assumptions, the system of Eqs. (1) and (2) can be rewritten in the cylindrical coordinates (r, x) as follows:

$$u = -\frac{K_{xx}}{\mu}\frac{\partial P}{\partial x}, \tag{3}$$

$$v = -\frac{K_{rr}}{\mu}\frac{\partial P}{\partial r}, \tag{4}$$

$$\frac{\partial u}{\partial x} + \frac{1}{r}\frac{\partial (rv)}{\partial r} = 0, \tag{5}$$

where r and x are the radial and axial coordinates, as shown in Fig. 2. Substituting Eqs. (3) and (4) into Eq. (5) yields an elliptic equation for pressure

$$K_{xx}\frac{\partial^2 P}{\partial x^2} + \frac{K_{rr}}{r}\frac{\partial}{\partial r}\left(r\frac{\partial P}{\partial r}\right) = 0. \tag{6}$$

The following boundary conditions for pressure are imposed:

$$P|_{\Gamma_t} = P_\infty(t, x, r),$$
$$P|_{\Gamma_b} = P_g(V_b) - P_\sigma, \tag{7}$$

where Γ_t and $\Gamma_b(t)$ are the tow and gas bubble surfaces, respectively, $P_\infty(t, x, r)$ is the external pressure distribution around the tow, which can be obtained by solving the macroscopic flow in the inter-tow region, $P_g(V_b)$ is the pressure inside the gas bubble, which is a function of the bubble volume V_b, and P_σ is pressure change because of the capillary effects. As shown in Pillai and Advani (1996), the capillary pressure for porous medium can be evaluated as follows:

$$P_\sigma = \frac{4\gamma\varepsilon_f \cos\theta}{d_f}, \tag{8}$$

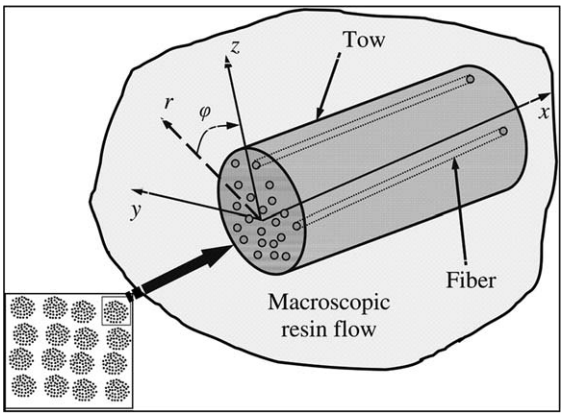

Fig. 2. Schematic of the physical intra-tow flow in a single fiber bundle.

where d_f is the diameter of an individual fiber, ε_f is the fiber volume fraction, θ is the contact angle, γ is the coefficient of surface tension. To close Eqs. (6) and (7), an equation of state for the gas entrapped inside the tow is required. The equation of state used in the present analysis is described in the next section.

The propagation of the resin front inside the fiber tow is a time-dependent problem. Because the vapor/resin interface location varies in time, Eqs. (6) and (7) should be solved as a moving boundary problem. To further simplify the problem, the following assumptions can be made: (1) K_{xx}/L^2 is much less than K_{rr}/r_t^2, where L and r_t are the tow length and radius, respectively; (2) the tow characteristic size is much smaller that the length scale on which the significant pressure changes occur in the inter-tow region; (3) the gas bubble entrapped inside the tow does not move with the macroscopic resin flow and always remains inside the tow, (4) the characteristic time scale of the vapor–liquid phase transition is much less than the tow impregnation time. Under the above assumptions, Eqs. (6) and (7) are simplified to

$$\frac{K_{rr}}{r}\frac{\partial}{\partial r}\left(r\frac{\partial P}{\partial r}\right)=0, \tag{9}$$

$$P|_{r=r_b(t)}=P_g(r_b)-P_\sigma, \quad P|_{r=r_t}=P_\infty(t), \tag{10}$$

where K_{rr} is the permeability coefficient in the radial direction, P_g is a function of the bubble radius, and P_∞ is a constant in space. The system of coordinates for the intra-tow flow perpendicular to the tow is shown in Fig. 3.

The radial permeability coefficient in Eq. (9), which depends on both the fiber packing and the fiber diameter, is evaluated by using the Kozeny–Carman equation (see, e.g., Kaviany, 1995)

$$K_{rr}=\frac{d_f^2(1-\varepsilon_f)^3}{36C_k\varepsilon_f^2},$$

where ε_f is the fiber volume fraction, d_f is the fiber diameter, and C_k is the Kozeny constant. The Kozeny coefficient for the flow perpendicular to fibers is set to be 11 as recommended in Lam and Kardos (1991). Assuming that fibers in the tow are hexagonally packed cylinders as shown in Fig. 4, the fiber volume fraction can be evaluated as follows:

$$\varepsilon_f=1-\frac{\pi}{2\sqrt{3}\left(1+\frac{\delta}{d_f}\right)},$$

where δ is the average distance between fibers inside the tow.

Eqs. (9) and (10) can readily be integrated to give the pressure distribution in the intra-tow resin flow region:

$$P(t,r)=c_1(t)\ln r+c_2(t), \tag{11}$$

where the "constants" c_1 and c_2 are found from the boundary conditions (10):

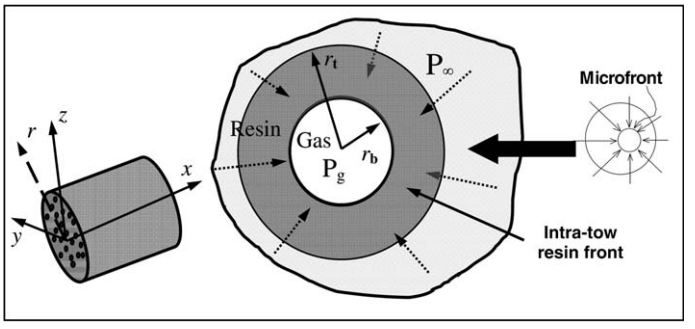

Fig. 3. The system of coordinates for the intra-tow flow perpendicular to the tow.

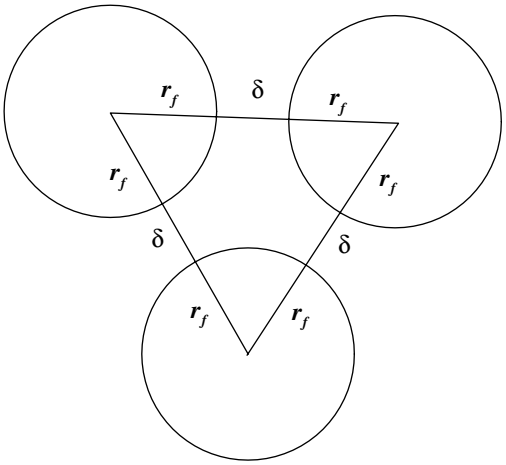

Fig. 4. Hexagonal fiber packing inside a fiber tow.

$$\begin{cases} c_1 \ln r_t + c_2 = P_\infty(t), \\ c_1 \ln r_b(t) + c_2 = P_g(r_b) - P_\sigma. \end{cases} \tag{12}$$

Eqs. (3)–(5) are valid not only in the microscopic resin flow, but also at the interface between the resin and the gas bubble. Hence, the same set of equations can be used to determine the bubble radius dynamics.

To find a relation between the gas bubble radius and the resin front velocity, let us estimate the rate of change of the entrapped gas volume V_b. On one hand, taking into account that the tow porosity is uniform, one can write

$$\frac{dV_b}{dt} = \varepsilon \frac{dV_t}{dt} = 2\varepsilon\pi r_b \frac{dr_b}{dt}, \tag{13}$$

where ε is the tow porosity, V_t is the total volume of the gas bubble including the volume of both fibers and gaps between them. On the other hand, the same quantity can be evaluated by using the Darcian resin front velocity v as follows:

$$\frac{dV_b}{dt} = S_t v = 2\pi r_b v, \tag{14}$$

where S_t is the total area of the gas bubble surface. The above equation has been derived using the fact that the Darcy velocity v is obtained by averaging the resin velocity over the total cross-section area including the area of pores and fibers. Setting Eqs. (13) and (14) equal to each other, the following equation for the gas bubble radius $r_b(t)$ can be obtained:

$$\frac{dr_b}{dt} = \frac{v}{\varepsilon}, \tag{15}$$

where v is the fluid radial velocity component at the resin/gas interface inside the tow.

Substituting Eq. (4) into Eq. (15), calculating the radial pressure gradient component from Eqs. (11) and (12), and evaluating all the equations at $r = r_b(t)$, the following equation for the gas bubble radius can be derived:

$$\frac{dr}{dt} = -\frac{K_{rr}}{\varepsilon\mu} \frac{P_\infty(t) + P_\sigma - P_g(r)}{r \ln\left(\frac{r_1}{r}\right)}. \tag{16}$$

Eq. (16) describes the gas bubble dynamics, which strongly depends not only on the pressure field outside the fiber bundle and the capillary effects, but also on the behavior of gas inside the bubble. If the sum of the exterior and capillary pressures exceeds the pressure inside the bubble, resin penetrates inside the fiber bundle,

thus removing the fluid from the advancing macroscopic flow into the tow. As the fluid impregnates the tow, the gas bubble radius reduces reaching its steady-state value when the pressure inside the gas bubble comes into equilibrium with the pressure outside the fiber bundle and the capillary pressure. If the steady-state gas bubble radius is non-zero, it indicates the potential for void formation.

In closed mold cavities, it is likely that gas entrapped inside voids consists of air, water vapor, and resin vapor. The thermodynamic behavior of this multi-component mixture is required to determine the $P_g(r)$ term in Eq. (16). In this work, the void formation and the intra-tow flow behavior are analyzed based on the Peng–Robinson equation of state which takes into account the vapor–liquid transition in the multi-component mixture. The detailed description of this equation of state is presented next.

3. The Peng–Robinson equation of state

In contrast to the existing void formation models which assume that the gas entrapped inside fiber tows behaves as a perfect gas, the new model takes into account the liquid–vapor transition processes that occur in the multi-component gas mixture under high pressures. In the present analysis, only the main components of the gas mixture, such as resin and water vapors, are considered. If the pressure exceeds the dew pressure of the mixture, then the resin vapor inside the void starts to condense into the fluid, lowering the gas pressure in the bubble. As a result, the void radius decreases, thus increasing the gas pressure in the void. To take into account this complicated physical phenomenon associated with the gas–liquid phase transition, an equation-of-state method is used. Assuming that for all the components, the liquid and gas phases stand in local thermodynamic equilibrium at each moment of time, an algebraic relationship between pressure, volume, and temperature can be obtained by adjusting the coefficients in this equation to ensure good fits with experimental data. With the equation of state, one can determine the density of each component for given pressures, temperatures, and compositions. In addition, the fugacity of each component in the mixture can be determined from the equation of state, which provides a basis for imposing the Gibbs constraints to calculate the compositions and overall mole fractions of each coexisting component.

There are several equations of state available in the literature, which can be used for gas–liquid systems (Sandler, 1999). In the present study, we use the Peng–Robinson equation of state (Peng and Robinson, 1976) to describe the behavior of multiphase mixtures at high pressures (0.5–3 MPa) and relatively low temperatures (300–350 K). This equation of state can be written in the following form:

$$P = \frac{RT}{\upsilon - b} - \frac{a(T)}{\upsilon(\upsilon + b) + b(\upsilon - b)}, \tag{17}$$

where υ is the molar volume, T is the temperature (K), $R = 8.314\ \mathrm{J\ mol^{-1}\ K^{-1}}$ is the universal gas constant, $a(T)$ and b are empirical parameters chosen to guarantee that the equation satisfies the critical-point properties. Eq. (17) can be rewritten in the form of a cubic polynomial

$$Z^3 - (1 - B)Z^2 + (A - 3B^2 - 2B)Z - (AB - B^2 - B^3) = 0, \tag{18}$$

where

$$A = \frac{a(T)P}{R^2T^2}, \quad B = \frac{bP}{RT}, \quad Z = \frac{P\upsilon}{RT}.$$

The compressibility factor Z measures the deviation of the mixture from ideal behavior. For a pure component, the parameters a and b are defined as follows:

$$a(T) = 0.45724\frac{R^2T_c^2}{P_c}\left[1 + (0.37464 + 1.54226\omega - 0.26992\omega^2)\left(1 - \sqrt{\frac{T}{T_c}}\right)\right]^2, \tag{19}$$

$$b = 0.07780\frac{RT_c}{P_c}, \tag{20}$$

where P_c and T_c are the critical pressure and temperature, respectively, and ω is acentric factor.

The same Eqs. (17) and (18) are valid for a mixture of several components. However, in this case, the coefficients a and b are calculated by using mixing rules which represent these coefficients in terms of composition and pure component parameters. In this work, the van der Waals mixing rules are used to determine the parameters a and b of the mixture:

$$a = \sum_{i=1}^{N} \sum_{j=1}^{N} x_i x_j (1 - k_{ij}) \sqrt{a_i a_j}, \tag{21}$$

$$b = \sum_{i=1}^{N} x_i b_i, \tag{22}$$

where a_i and b_i are the parameters for a pure component i defined by Eqs. (19) and (20) using the critical parameters P_c, T_c and ω for the component i, N is the number of components in the mixture, k_{ij} is the binary interaction parameter which is introduced to obtain better agreement with experimental data.

To determine the compressibility factors of each existing phase, the cubic equation (18) should be solved, which yields one or three roots, depending on the number of phases in the system. In the two-phase region, the largest root corresponds to the compressibility factor of the vapor whereas the smallest root corresponds to that of the liquid. The vapor–liquid equilibrium of the multi-component mixture is calculated by using the Gibbs equal-fugacity constraint for each component. The fugacity coefficient of component k calculated using the Peng–Robinson equation of state is given by

$$\ln \frac{f_k}{x_k P} = \frac{b_k}{b}(Z - 1) - \ln(Z - B) - \frac{A}{2\sqrt{2}B} \left(\frac{2\sum_{i=1}^{N} x_i (1 - k_{ik}) \sqrt{a_i a_k}}{a} - \frac{b_k}{b} \right) \ln \left(\frac{Z + (1 + \sqrt{2})B}{Z + (1 - \sqrt{2})B} \right), \tag{23}$$

where f_k is the fugacity coefficient of component k. Using the Gibbs equal-fugacity constraints

$$f_k^{\mathrm{v}} = f_k^{\mathrm{l}}, \tag{24}$$

the compositions of each phase in the mixture can be determined. The superscripts "v" and "l" denote the vapor and liquid phases, respectively. Eqs. (24) are highly nonlinear and should be solved by some approximate iterative technique, e.g., the Newton's method. To reduce the computational expenses associated with the coupled solution of the flow equation (16) and the vapor–liquid equilibrium constraints (24), a family of equilibrium states at various saturation pressures has been calculated beforehand by using the Peng–Robinson equation of state for the given mixture. During the integration of Eq. (16), the relation between the void pressure and its volume is obtained by interpolating between the equilibrium states calculated for this multi-component mixture. This approach allows us to reduce significantly the computational time while maintaining high accuracy of the numerical solution.

4. Results and discussion

The governing Eq. (16) is integrated in time by using a low-storage, explicit fourth-order Runge–Kutta method developed in Kennedy et al. (2000). The simulations are all run at the maximum stable time step. The Runge–Kutta scheme has an error estimator that monitors the temporal error per time step. For all the simulations presented, the temporal error based on the L_∞ norm of the radius variable was less than 10^{-8}. To validate the code, we compared the steady-state radius obtained numerically with its exact value calculated analytically. Actually, the exact void radius can be calculated from Eq. (16). When the system reaches its steady-state regime, the left hand side in Eq. (16) becomes equal to zero, thus resulting in the following nonlinear equation for the void radius:

$$P_\infty + P_\sigma - P_g(r) = 0. \tag{25}$$

Taking into account the fact that the first two terms in Eq. (25) do not depend on the void radius, the above equation can readily be solved either analytically in the case of the equation of state for a perfect gas or by using the Newton's method if $P_g(r)$ is given by the Peng–Robinson equation of state. The error obtained using the equation of state for a perfect gas at different exterior pressures is shown in Table 1. As one can see from

Table 1
Error in the steady-state void radius obtained using the equation of state for a perfect gas for different external pressures

External pressure P_∞ (MPa)	Steady-state radius, $\frac{r}{r_t}$	Error, $\left\lvert\frac{r-r_{ex}}{r_{ex}}\right\rvert$
2.0	0.22258	8.28×10^{-10}
1.0	0.31333	1.78×10^{-9}
0.5	0.43913	3.48×10^{-9}

the results presented in Table 1, the numerical error is of the order of machine zero for all the test cases considered. Similar behavior remains valid for the Peng–Robinson equation of state.

The advancing macroscopic resin front penetrates inside a fiber bundle, while it flows around the tow. As a result, the initial bubble radius is actually smaller than that of the tow. In all simulations presented here, the initial radius is taken to be 99% of the tow radius. To determine the effect of the vapor–liquid phase transition on the void formation dynamics, the void radius and pressure are compared with those obtained using the equation of state for a perfect gas.

The composition and overall mole fractions of each co-existing phase in real resin mixtures are not readily available and should be measured experimentally. Furthermore, the critical pressures, critical temperatures, acentric factors, and binary interaction parameters of resin systems used in LCM processes should be determined to use the Peng–Robinson equation of state. In the present study, we assume that the thermodynamic properties of the resin vapor are similar to those of propylene (C_3H_6). Because of the presence of moisture in both resin and air, it is also natural to assume that multi-component gas mixture entrapped inside voids could contain water vapor. Therefore, we consider the time-dependent behavior and collapse of voids for the following three systems: (1) resin and air, (2) liquid resin and its vapor, and (3) a binary mixture of resin, water, and their vapors. The critical parameters for water and propylene are given in Table 2. In the case of the binary mixture, the initial molar fraction of the resin vapor has been chosen to be 95%. For all the test cases considered, the resin temperature is assumed to be constant and equals 310 K. In the case of pure air, the phase transition does not occur, and the gas behavior is described by using the equation of state for a perfect gas. Several important factors that would influence the LCM processing conditions are considered, and correlations to the observations in real liquid composite molding processes are discussed below.

4.1. Effect of external pressure

As has been observed in liquid composite molding processes, the concentration of voids is higher near the vent and low pressure regions inside complex mold cavities. Even in simple quasi-one-dimensional flow configurations, the size of voids as observed using micrographs are larger near the far end from the injection inlet. To check whether or not the new model can predict this behavior, the effect of external pressure on the transient evolution and collapse of voids inside fiber bundles is considered. The intra-tow flow under various external pressure conditions is solved by using the present model to simulate the macroscopic pressure variation across different regions in a complex mold geometry. Time histories of the non-dimensional void radius obtained under exterior pressure conditions of 0.5 and 2 MPa are shown in Fig. 5. The exterior pressure, $P_\infty = 2$ MPa, simulates a region near the injection port, whereas $P_\infty = 0.5$ MPa corresponds to a region located closer to the vent. The initial gas pressure is taken to be normal atmospheric pressure of 0.1 MPa. For all the equations of state considered, the steady-state void radius decreases if the external pressure increases. The transient time to reach the steady-state regime also becomes smaller as the pressure around the tow increases. This is consistent with observations in liquid composite molding processes, which indicate

Table 2
The critical pressure, critical temperature, and acentric factor for water and propylene

	P_c (MPa)	T_c (K)	ω
Water	22.12	647.3	0.344
Propylene	4.613	364.8	0.142

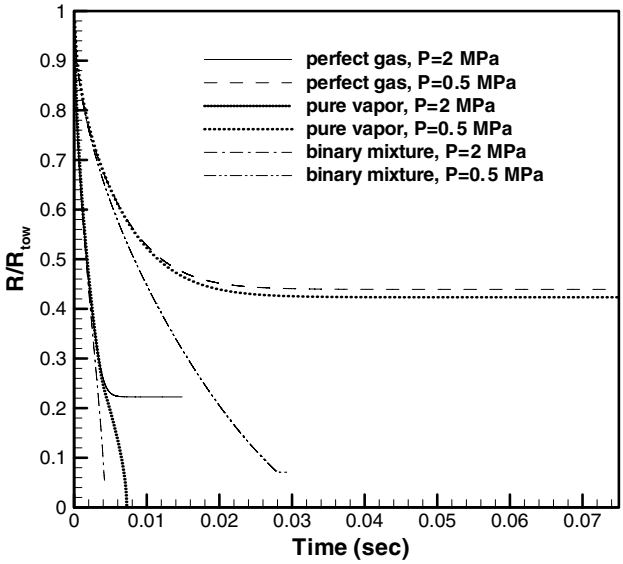

Fig. 5. Time histories of the void radius obtained using the perfect gas, pure vapor, and binary mixture models at the external pressures of 0.5 and 2 MPa.

that the void concentration and sizes are significantly smaller in those regions of a composite part where higher flow pressures are experienced during the process.

It should be emphasized that the liquid–vapor phase transition has a very strong effect on the void radius dynamics, as seen in Fig. 5. In contrast to the ideal gas case, the condensation and vaporization processes inherent in the resin vapor and water/resin binary mixture systems drastically change the gas behavior if the void pressure exceeds its saturation value. As the void radius decreases, the pressure inside the gas bubble increases and reaches the dew point of the resin vapor. It leads to the formation of liquid resin, thus lowering the gas pressure inside the bubble. As a result, the void radius reduces, causing the gas pressure inside the bubble to increase, thus initiating the vapor/liquid phase transition process again. The liquid resin formation continues until the entire resin vapor condensates into liquid resin surrounding the void. In the consequence of this, the void dissolves completely if, initially, it consists of only pure resin vapor, and there is no moisture in the system. However, as seen in Fig. 5, if the gas entrapped inside the void initially contains the mixture of resin and water vapors, the steady-state void radius is much smaller than that of the ideal gas model, but not equal to zero, because of the presence of water and its vapor inside the void. Similar to the ideal gas case, the void formation time in the pure resin vapor and binary mixture cases reduces as the exterior pressure becomes larger.

The pressure built-up inside the gas bubble correlates to the void radius dynamics considered above. When the sum of the external and capillary pressures is equal to or less than the internal pressure inside the bubble, the resin front velocity becomes zero, and further flow inside the tow is not possible. Fig. 6 shows the transient behavior of the pressure inside the void, which corresponds to the time history of the void radius depicted in Fig. 5. Note that the plot for the pure vapor case in Fig. 6 has two kinks. The first kink that occurs approximately at 4.4 ms corresponds to the beginning of the phase transition. The second kink at 7.2 ms indicates the end of the vapor condensation process. At this moment, there is no resin vapor left inside the bubble. As a result, the system behaves as an incompressible fluid, causing the rapid increase in the pressure. Comparing Figs. 5 and 6, one can see that as soon as the pressure gradient at the gas/liquid interface vanishes, the intra-tow flow ceases to exist, and the void radius reaches its minimum value.

4.2. Effect of resin viscosity

The resin viscosity has the strong effect on the flow velocity and the infusion time during LCM processes. Usually, resin systems are heated to reduce the viscosity and to improve the impregnation process. To evaluate

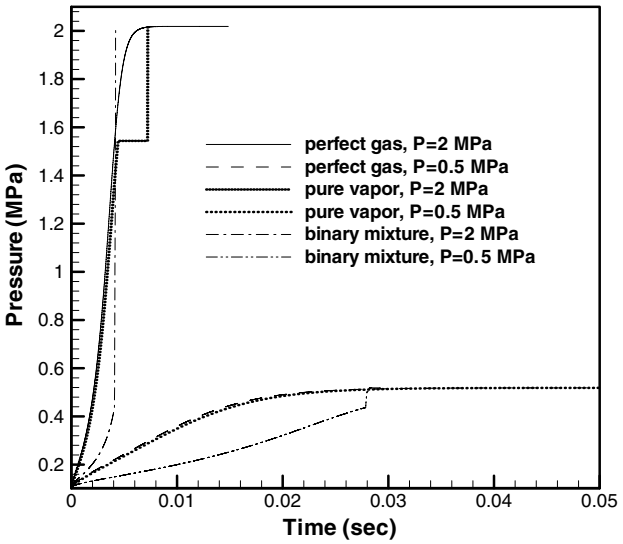

Fig. 6. Time histories of the void pressure obtained using the perfect gas, pure vapor, and binary mixture models at the external pressures of 0.5 and 2 MPa.

the effect of the resin viscosity on the void radius dynamics described by the present model, the intra-tow flow at different resin viscosities is considered. Fig. 7 shows time histories of the void radius obtained using three resin viscosity values (0.1 kg/ms, 0.09 kg/ms, and 0.11 kg/ms) for both the perfect gas and binary mixture models at the external pressure of 2 MPa. As one can see in Fig. 7, for each equation of state used, the steady-state void radius remains unchanged for all the resin viscosities considered. However, the void formation time in both cases becomes smaller as the resin viscosity decreases. This effect can also be seen in Fig. 8 which shows time histories of the void pressure obtained under the same conditions. As the resin viscosity increases, the microscopic front velocity decreases, thus resulting in a slower pressure build-up inside the void as compared with those corresponding to the lower viscosity values. Another conclusion that can be drawn form this comparison is a significant difference in the pressure behaviors obtained with the perfect gas and binary mixture models. The presence of water in the system significantly reduces the saturation pressure of

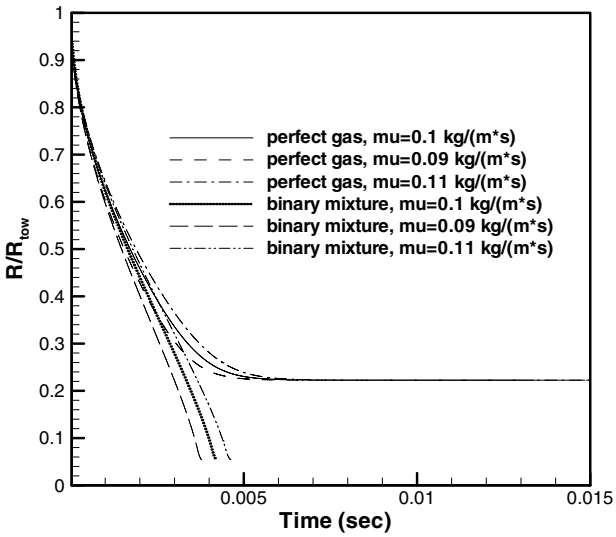

Fig. 7. Effect of the resin viscosity on the void radius obtained using the perfect gas and binary mixture models.

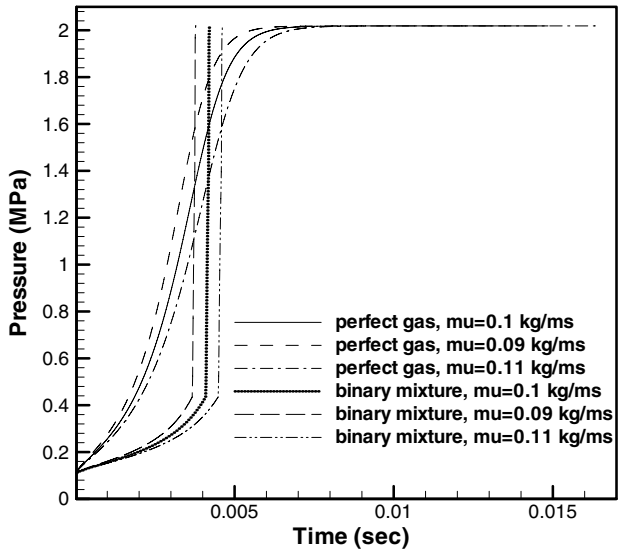

Fig. 8. Effect of the resin viscosity on the void pressure obtained using the perfect gas and binary mixture models.

the binary mixture, which is slightly higher than the normal atmospheric pressure. As a result, the phase transition starts practically at the beginning of the tow impregnation process, thus considerably lowering the pressure inside the void as compared with that in the perfect gas case. When the entire resin and water vapors have condensed, the void pressure rapidly increases, because the water remaining inside the void is practically incompressible. The jump in the binary mixture pressure values in Fig. 8 indicates the end of the phase transition process.

4.3. Effect of tow radius

As follows from Eq. (16), the characteristic time scale associated with the microscopic flow is of the order of $t_c = \frac{\mu r_t^2 \varepsilon}{K_m P_0}$, where r_t is the tow radius, ε is the tow porosity, and P_0 is the gas pressure at the initial moment of time. The above formula shows that the characteristic void formation time is quadratic in the tow radius if the fiber radius and the intra-tow fiber volume fraction remain unchanged. To check whether or not the time taken to reach the equilibrium is a quadratic function of the tow radius, the void formation time obtained numerically by using the equations of state for both the perfect gas and binary mixture models are presented in Table 3. As expected, the void formation time calculated numerically perfectly follows the theoretically predicted quadratic law. Three cases corresponding to different tow radii of 1 mm, 0.5 mm, and 1.5 mm at the same external flow pressure of 2.0 MPa are considered to analyze the effect of the tow radius on the void formation time. Fig. 9 shows that for each equation of state, the non-dimensional steady-state void radius is the same for all the tow radii considered. Note, however, that as r_t decreases, the actual physical size of the void decreases proportionally to the tow radius. Similar behavior is observed for the gas pressure inside the void, which is shown in Fig. 10. Note that in the case of the binary mixture, the time for which the void pressure reaches its equilibrium value is about two times less than that of the perfect gas. The main reason for such a behavior is that the time the water and resin vapors take to completely condense is much less than the time it takes for the pressure of a perfect gas inside the void to reach the equilibrium with the exterior and capillary pressures.

Table 3
The void formation time obtained at different tow radii

	$r_{t1} = 0.05$ mm	$r_{t2} = 0.1$ mm	$r_{t3} = 0.15$ mm	t_{c2}/t_{c1}	t_{c3}/t_{c1}
Perfect gas	2.426 ms	9.702 ms	21.830 ms	4	9
Binary mixture	1.049 ms	4.195 ms	9.439 ms	4	9

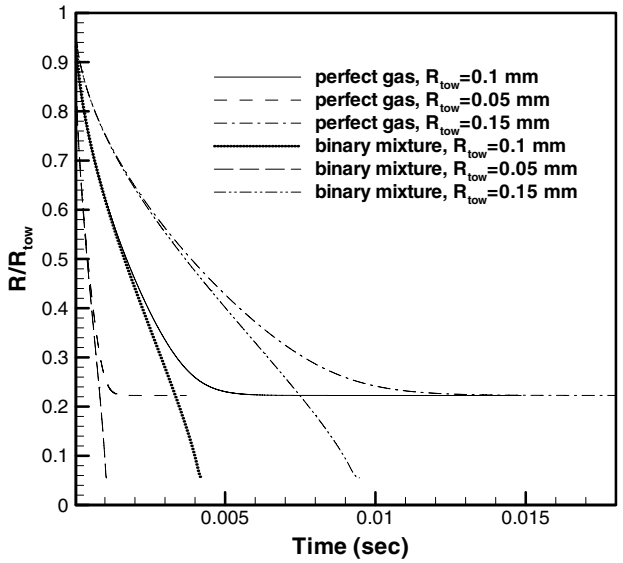

Fig. 9. Effect of the tow size on the void radius dynamics obtained using the perfect gas and binary mixture models.

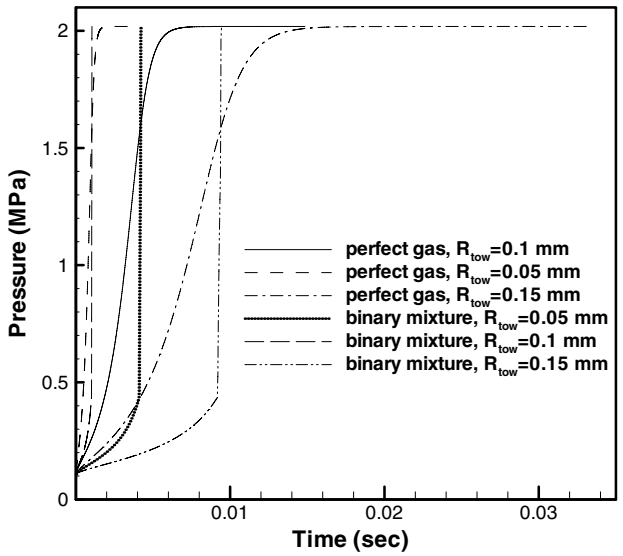

Fig. 10. Effect of the tow size on the void pressure obtained using the perfect gas and binary mixture models.

4.4. Effect of the intra-tow fiber volume fraction

It is well known that the permeability coefficient strongly depends on the pore volume fraction of the porous medium in question. In the present analysis, the fiber bundle is considered as a porous medium, and its permeability coefficient K_{rr} is evaluated by using the Kozeny–Carmen formula, which is an essentially nonlinear function of the fiber volume fraction. To study the effect of the fiber volume fraction on void radius dynamics, three intra-tow fiber volume fraction values (0.4, 0.58 and 0.8) for a given tow radius are considered. Time histories of the void radius obtained using the equations of state for the binary mixture and a perfect gas are shown in Fig. 11. It should be noted that the void radius converges to the same value for all three intra-tow fiber volume fractions considered. This result is not surprising, because when the solution

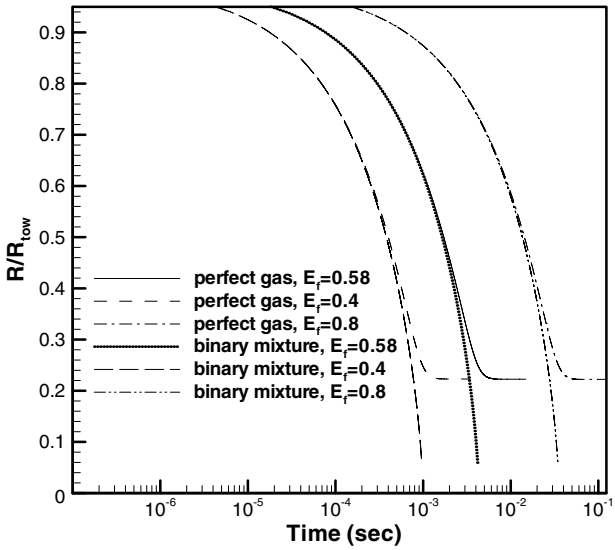

Fig. 11. Effect of the intra-tow fiber volume fraction on the void radius obtained using the perfect gas and binary mixture models.

approaches the steady-state regime, the left hand side of Eq. (16) vanishes, thus nullifying the pressure gradient on the right hand side of the equation. Because in this case, the permeability coefficient in front of the pressure gradient term can be canceled, and the capillary pressure is negligibly small, the steady-state solution depends on neither K_{rr} nor the fiber volume fraction, which can clearly be seen in Fig. 11. Another observation is that the time taken to reach the equilibrium becomes significantly larger, as the fiber volume fraction increases. The reason for such a behavior is that the intra-tow permeability coefficient becomes smaller for larger values of the fiber volume fraction, thus reducing the front velocity, which results in a slower propagation of the microscopic resin front inside the tow. Time histories of the pressure inside the void are shown in Fig. 12. Similar to the void radius dynamics presented in Fig. 11, the steady-state value of the void pressure is independent of the fiber volume fraction, whereas the void formation time increases by two orders of magnitude as the fiber volume fraction increases from 0.4 to 0.8.

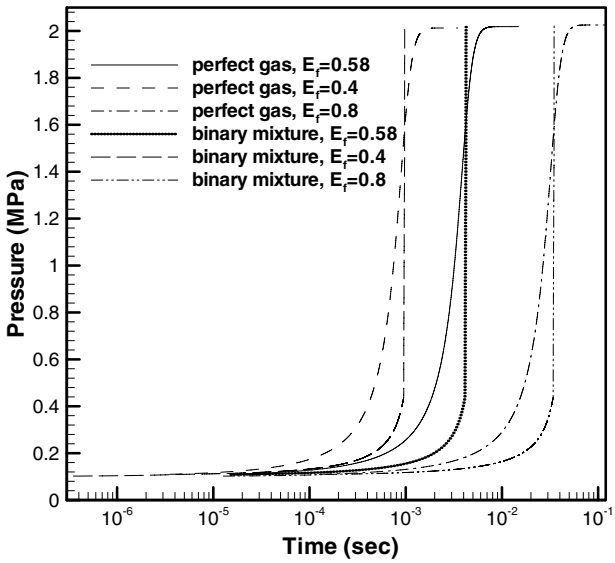

Fig. 12. Effect of the intra-tow fiber volume fraction on the void pressure obtained using the perfect gas and binary mixture models.

5. Conclusions

The model describing the microscopic isothermal flow perpendicular to a fiber tow under a high external fluid pressure, which takes into account the phase transition phenomenon occurring in gas entrapped inside the tow, has been developed and implemented. The time-dependent intra-tow impregnation process is considered for the following three liquid/gas systems: (1) resin and pure air, (2) resin and pure resin vapor, and (3) the binary mixture of the resin–water system and their vapors. In the first case, the air entrapped inside the tow is described by the equation of state for a perfect gas. To simulate the vapor–liquid phase transition inherent in the multiphase systems, the Peng–Robinson equation of state is used. In the test simulations presented, the thermodynamic properties of the resin are assumed to be similar to those of propylene. Parametric studies have been conducted to analyze the effects of exterior pressure, resin viscosity, tow radius, and fiber volume fraction. As expected, for all the cases considered, the condensation of the resin and water vapors, which occurs during the microscopic impregnation process, considerably reduces the steady-state void size as compared with that of the perfect gas. Another important conclusion that has been drawn from this study is that the void formation time is much smaller if the real gas effects are taken into account. As follows from the numerical results presented, the void dynamics strongly depends on the thermodynamic properties of both the entrapped gas and surrounding liquid. The results obtained with the new model demonstrate a good qualitative agreement with those observed in the experiments. However, to quantitatively predict the flow inside a fiber bundle, the thermodynamics properties (such as the critical temperature and pressure, acentric factor, and the binary interaction coefficients) of realistic resin systems and realistic volatile gases should be used. Although the model presented here is an important step towards a better understanding of the physical phenomena associated with the void formation at the intra-tow scale, further development of models for the coupled simulation of the macro–micro flow including the multidimensional, thermal, and cure effects is required. The development of this full-scale model is the focus of ongoing work.

References

Bruschke, M.V., Advani, S.G., 1990. A finite element/control volume approach to mold filling in anisotropic porous media. Polymer Composites 11, 398–405.

Kaviany, M., 1995. Principles of Heat Transfer in Porous Media. Springer-Verlag, New York.

Kennedy, C.A., Carpenter, M.H., Lewis, R., 2000. Low-storage, explicit Runge–Kutta schemes for the compressible Navier–Stokes equations. Applied Numerical Mathematics 35, 177–219.

Lam, R.C., Kardos, J.L., 1991. The permeability and compressibility of aligned and cross-plied carbon fiber beds during processing of composites. Polymer Engineering 31, 1064.

Lin, R.T., Lee, L.J., Liou, M.J., 1993. Mold filling and curing analysis in liquid composite molding. Polymer Composites 14, 71–81.

Lundstrom, T.S., 1997. Measurement of void collapse during resin transfer molding. Composites Part A 28, 201–214.

Mohan, R.V., Ngo, N.D., Tamma, K.K., 1999. On a pure finite-element-based methodology for resin transfer molds filling simulations. Polymer Engineering and Science 39, 26–43.

Ngo, N., Mohan, R.V., Chung, P.W., Tamma, K.K., Shires, D.R., 1998. Recent developments encompassing non-isothermal/isothermal liquid composite process modeling/analysis: Physically accurate, computationally effective and affordable simulations and validations. Journal of Thermoplastic Composite Materials 11, 493–532.

Parnas, R.S., Phelan Jr, F.R., 1991. The effect of heterogeneous porous media on mold filling in resin transfer molding. SAMPE Quarterly 23, 53–60.

Peng, D.-Y., Robinson, D., 1976. A new two-constant equation of state. Industrial & Engineering Chemistry Fundamentals 15, 53–64.

Pillai, K.M., Advani, S.G., 1996. Wicking across a fiber bank. Colloid and Interface Science 183, 100–110.

Pillai, K.M., Advani, S.G., 1998. A model for saturated flow in woven fiber preforms during mold filling in resin transfer molding. Journal of Composite Materials 32, 1753–1783.

Sandler, S.I., 1999. Chemical and Engineering Thermodynamics. John Wiley & Sons, Inc., New York.

Trouchu, T., Gauvin, R., Gao, D., 1993. Numerical analysis of the resin transfer molding process by the finite element method. Advances in Polymer Technology 12, 329–342.

Wood, J.R., Bader, M.G., 1994. Void control for polymer–matrix composites (1): Theoretical and experimental methods for determining the growth and collapse of gas bubbles. Composites Manufacturing 5, 139–147.